Effects of volume fraction and particle shape on the rheological properties of oblate spheroid suspensions

Junwei Guo,[1] Qi Zhou*,[1] and Ron Chik-Kwong Wong[1]

[1]*Department of Civil Engineering, University of Calgary*

2500 University Drive NW, Calgary, Alberta T2N 1N4, Canada

(*Electronic mail: qi.zhou1@ucalgary.ca)

(Dated: 22 July 2021)

Coupled lattice Boltzmann and discrete element methods were employed to investigate the rheological properties of oblate spheroid suspensions in a Newtonian fluid. The volume fraction of the particles is varied, along with the particle aspect ratio. As the particle shape is varied from sphere to oblate, we observe an increase of the relative viscosity, as well as an increase of the particle contacts and the contact distance. The more oblate particles in denser suspensions are observed to reorient systematically subject to the shear flow. We recast the viscosity data using the Krieger–Dougherty formula and report the modified Einstein coefficients.

The rheology of non-Brownian suspensions of spherical particles has been the topic of extensive studies and been reviewed elsewhere[1–3]. The bulk rheological properties of these suspensions is the manifestation of physical processes occurring at the particle scale, such as the fluid-particle interactions and inter-particle interactions. One of the key parameters is the volume fraction of particles, ϕ, which has a direct impact on the viscosity of the suspension[4,5]. With a few exceptions[6–10], most studies in the literature have been focused on spherical particle suspensions. In the present study, we focus instead on the ellipsoidal particle suspensions and investigate the effects of ϕ, as well as the particle shape, on the rheological properties of these suspensions.

In a simple shear flow, the relative viscosity η_r of the suspension is defined as

$$\eta_r = \frac{\Sigma_{12}}{\eta_f \dot{\gamma}}, \tag{1}$$

where Σ_{12} is a component of the suspension stress tensor $\mathbf{\Sigma}$, η_f is the viscosity of the suspending fluid, and $\dot{\gamma}$ is the imposed bulk shearing rate. Here, the 1, 2, and 3 directions correspond to the flow, velocity gradient, and vorticity directions of the shear flow, respectively. The first and second normal stress difference coefficients are defined as

$$N_1^* = \frac{\Sigma_{11} - \Sigma_{22}}{\eta_r \eta_f \dot{\gamma}}, \qquad \text{and} \qquad N_2^* = \frac{\Sigma_{22} - \Sigma_{33}}{\eta_r \eta_f \dot{\gamma}}, \tag{2}$$

respectively, which measure the loss of isotropy in the normal stresses. The rheology of the suspension can largely be described by η_r, N_1^*, and N_2^*, which are the focus of this paper.

The correlation between η_r and ϕ has been well known for sphere suspensions. In the very dilute regime, η_r varies linearly with ϕ, according to Einstein[4]. Other viscosity laws were proposed (see Table I) and have enjoyed considerable success in matching experimental data (see Fig. 4 of Guazzelli and Pouliquen[3]) for spherical particle suspensions. For the normal stress differences, studies on sphere suspensions suggest that N_2^* is generally negatively signed, whereas N_1^* exhibits more uncertainty and can be either positive or negative.

The motion of an ellipsoidal particle in a shearing flow was studied by Jeffery[13]. Utilizing Jeffrey's solution, Mueller et al.[8] combined analytical and experimental work to investigate the viscosity of ellipsoidal (both oblate and prolate) particle suspensions. They reported empirical values for the maximum packing fraction, ϕ_m, and the Einstein coefficient, B. Numerical simulations were performed to study the viscosity of plate-like particle[14] and oblate particle suspensions[9]. The latter work reported values of η_r, N_1^*, and N_2^* of oblate spheroidal particle suspensions for ϕ up to 0.25. The algorithm used relies on Jeffrey's solution to prescribe the particle motions and

TABLE I: Some proposed correlations for the relative viscosity of sphere suspensions. $B = 2.5$ is the Einstein coefficient, and $\phi_m \approx 0.64$ is the maximum packing fraction for spheres.

Einstein (1906)	$\eta_r = 1 + B\phi$
Maron and Pierce (1956)	$\eta_r = (1 - \phi/\phi_m)^{-2}$
Krieger and Dougherty (1959)	$\eta_r = (1 - \phi/\phi_m)^{-B\phi_m}$
Batchelor and Green (1972)	$\eta_r = 1 + B\phi + 6.95\phi^2$

introduces equivalent spherical surfaces to approximate the spheroidal surfaces when calculating inter-particle interactions.

In this paper, we employ the lattice Boltzmann (LB) and discrete element (DE) methods to simulate the suspensions of oblate spheroidal particles. The fluid phase, whose motion is governed by Navier–Stokes equations, is solved by the LB method, while the solid phase is solved directly by the DE method. The volume fraction is varied (for ϕ up to 0.40), as well as the aspect ratio (α) of the oblate particles. The aim of the study is to investigate the effects of ϕ and α on the bulk rheological properties (such as η_r, N_1^*, and N_2^*) and quantify parameters (such as B) for oblate particle suspensions.

TABLE II: Material properties used in all simulations.

Particle density:	$\rho^p = 1200\,\mathrm{kg/m^3}$	Fluid density:	$\rho^f = 1000\,\mathrm{kg/m^3}$
Fluid viscosity:	$\nu^f = 1 \times 10^{-6}\,\mathrm{m^2/s}$	Young's modulus:	$E = 1 \times 10^6\,\mathrm{Pa}$
Poisson's ratio:	$\nu = 0.3$	Friction coefficient:	$\mu_s = 0.27$
Shearing rate:	$\dot{\gamma} = 1000\,\mathrm{Hz}$	Damping factor:	$c_n = 0.5$

The coupled LB and DE methods are employed to simulate the fluid-particle flow. The algorithm is implemented through an open-source software package known as *OpenLB*[15–17] which is capable of simulating arbitrarily shaped particles. Two-way coupling is implemented for the momentum exchange between the particles and fluid and is performed by the procedure developed by Krause *et al.*[15] enforcing the 'bounce-back' condition[18,19] at the particle-fluid boundary nodes. An efficient scheme for ellipsoidal particle contact detection proposed by Lin and Ng[20,21] is employed. The normal contact forces include Hertz's elastic force[22,23] and a small damping

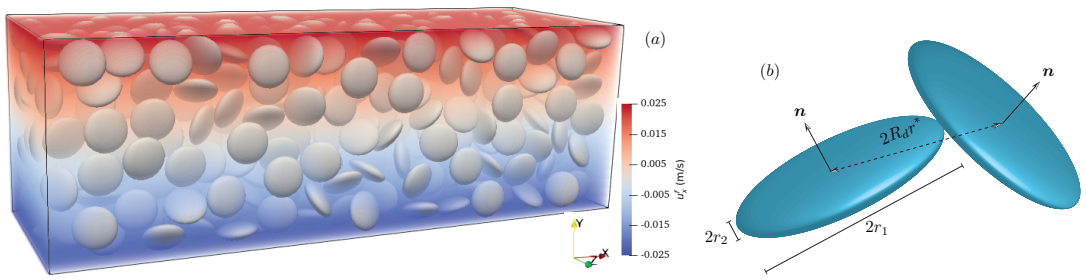

FIG. 1: (a) The initial position and orientation of the ellipsoidal particles ($\phi = 0.30$) in a fluid channel, and initial fluid velocity field shown by color. (b) A contacting particle pair. The distance between the particle centers is $2R_d r^*$, where r^* is the equivalent radius, $\sqrt[3]{r_1 r_1 r_2}$. The normal vector $\boldsymbol{n}$ is the unit vector in the direction of the symmetric axis.

force specifically designed for ellipsoidal particles[24]. The tangential contact force includes the Coulomb's friction force. The physical parameters pertinent to the particle contact model are summarized in Table II. The particle Reynolds number, $\mathrm{Re} \equiv \dot{\gamma}(r^*)^2/\nu^f$, is 0.014, which lies in the Stokes flow regime. The particle-to-fluid density ratio, ρ^p/ρ^f, is held constant at 1.2. Preliminary work done for $\rho^p/\rho^f = 2.7$ (not shown) suggests no significant variation of the rheological properties with the density ratio at this range, which is consistent with the observations by Thorimbert *et al.*[25] For the LB calculations, the D3Q15 lattice with the Bhatnagar–Gross–Krook operator (see e.g., Krüger[26]) is employed. Following two previous LB-based studies[15,25], no explicit lubrication force modeling is included in the LB-DE solver. A detailed documentation of the LB and DE methods for this specific configuration can be found in Chapter 3 of Guo[27].

TABLE III: Parameters for simulations. The volume of each particle in all simulations is fixed. Hence, for suspensions with a specific ϕ, the number of particles in the system is the same, regardless of the difference in shape.

$\alpha \equiv r_2/r_1$	r_1, r_2 (μm)	ϕ
0.4	5.00, 2.00	0.00 – 0.40
0.6	4.37, 2.73	
0.8	3.97, 3.17	
1.0	3.74, 3.74	

As shown in Fig. 1(a), simulations are performed for a $150\,\mu\mathrm{m} \times 50\,\mu\mathrm{m} \times 50\,\mu\mathrm{m}$ fluid channel.

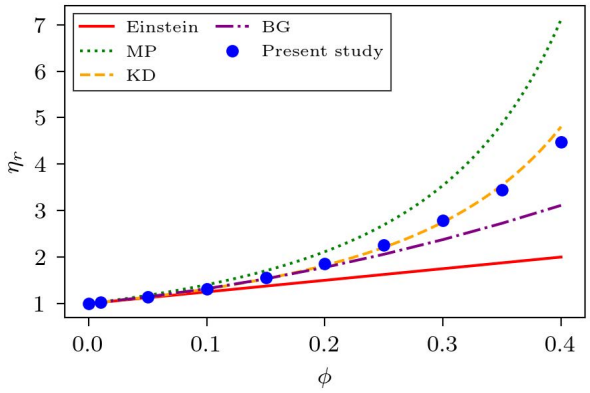

FIG. 2: Comparison of computed relative viscosity of spherical particle suspension ($\alpha = 1.0$) with viscosity laws (Table I) in the literature: Einstein[4], Maron and Pierce[11] (MP), Krieger and Dougherty[12] (KD), Batchelor and Green[5] (BG).

A plane Couette flow is set up by the top and bottom boundaries, and the flow is periodic in the x and z directions. The top ($y = 2h = 50\,\mu$m) and bottom ($y = 0$) walls move in opposite directions with a specific speed to create the imposed shearing rate $\dot{\gamma}$ (see Table II). The initial velocity field follows a linear profile, i.e., $\boldsymbol{u}^f(t=0) = (\dot{\gamma}(y-h), 0, 0)$. The initial position and orientation of the particles, which are randomized as much as possible, are generated by a program known as *Packing Ellipsoid 3*[28]. Four sets of simulations are performed, whose input parameters are tabulated in Table III. No effects of gravity are included in the simulations. As shown in Fig. 1(b), the diameter of the oblate particle along the symmetric axis is $2r_2$, and the equal diameter along the other axes is $2r_1$. The particle aspect ratio, $\alpha \equiv r_2/r_1$, is varied from 0.4 to 1.0 (the latter corresponds to a sphere). Ten simulations are run for each α, with ϕ varied from 0.00 to 0.40. Each simulation is run up to a time corresponding to $\dot{\gamma}t = 20$. An initial transient is typically observed in the statistics for $0 < \dot{\gamma}t < 5$. Hence, we regard $5 < \dot{\gamma}t < 20$ as the quasi-steady state and produce time-averaged statistics for this specific time window. During the quasi-steady state, an approximately linear velocity profile (as in the initial condition) is observed for the mean flow between the two walls. Upon conducting mesh convergence tests, we set the grid spacing at $0.5\,\mu$m, time step at 41.7 ns, and the dimensionless relaxation time at 1.0 for LB calculations[26]. The OpenLB program is executed on the *Cedar* cluster operated by Compute Canada. Each simulation takes approximately 10 days to run using 40 to 100 parallel processors, depending on the number of particles in the system. Detailed description of how the rheological parameters (Eqs. 1 and 2) are calculated from the results of the LB and DE calculations can be found in Chapter 2 of Guo[27].

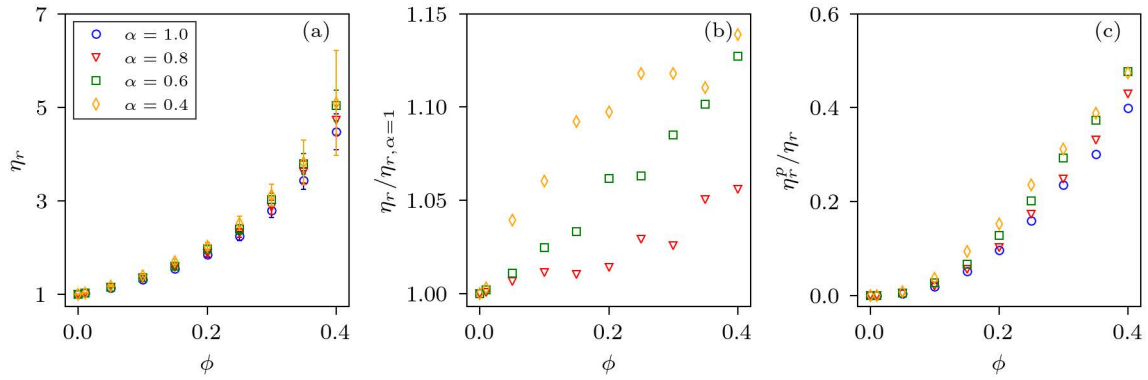

FIG. 3: (a) The relative viscosity η_r vs. ϕ. (b) The ratio of η_r to the sphere suspension viscosity $\eta_{r,\,\alpha=1}$ vs. ϕ. (c) The fraction of viscosity due to inter-particle interactions, η_r^p/η_r vs. ϕ.

The relative viscosity η_r of the spherical particle suspension (Eq. 1) is plotted against ϕ in Fig. 2. The results from our $\alpha = 1$ (sphere) simulation are compared with the viscosity laws (Table I). Our numerical results reproduce the expected trend between η_r and ϕ and are in general agreement with the Krieger–Dougherty (KD) formula[12]. In Fig. 3(a), the η_r vs. ϕ relation is shown all four cases of α. For all cases, η_r increases with ϕ. In Fig. 3(b), the ratio $\eta_r/\eta_{r,\,\alpha=1}$ is shown, where $\eta_{r,\,\alpha=1}$ is the relative viscosity of the spherical particle suspension at each ϕ. $\eta_r/\eta_{r,\,\alpha=1}$ is greater than unity for all $\alpha < 1$, suggesting that the oblate spheroid suspensions yield a higher viscosity than their spherical counterparts. The ratio also generally increases with ϕ. In Fig. 3(c), we focus on η_r^p, i.e., the component of η_r due to inter-particle interactions, which can be calculated from the contact stresslet outlined by Eq. 2.24 of Gallier *et al.*[23]. As expected, η_r^p makes up a larger portion of η_r as ϕ increases up to 0.40, as inter-particle collisions become more likely in a denser suspension.

Increased particle collisions may also result in anisotropy in the normal stresses. The normal stress difference coefficients N_1^* and N_2^* (Eq. 2) are plotted against ϕ in Fig. 4. Similar to the spherical particle suspension data compiled by Guazzelli and Pouliquen[3], the sign of N_1^* is inconclusive. As the particles become more oblate, the sign of N_1^* switches from positive to negative for the denser suspensions ($\phi \geq 0.20$). N_2^* appears to be negative for all cases, which is consistent with the sphere cases[3]. As compared to N_1^*, N_2^* seems less sensitive to α at a given value of ϕ. Particle collisions are expected to occur most frequently within the plane of shear[3], i.e., the x-y plane, which leads to a negative N_2^* – this seems to be the case regardless of the particle shape.

To visualize any reorientation of the particles subject to shearing, we perform equal area projection (EAP) (Sec. 3.3 of Fisher *et al.*[29]) to display the normal vector $\boldsymbol{n}$ of each particle on the x-z

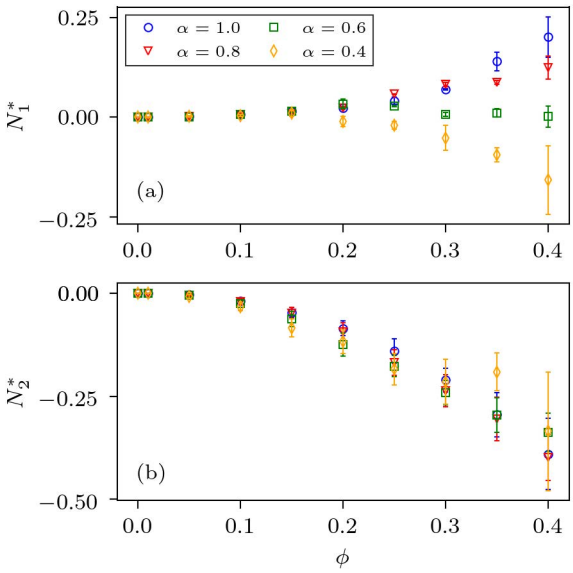

FIG. 4: First and second normal stress difference coefficients, (a) N_1^* and (b) N_2^*, vs. ϕ.

plane (Fig. 5). EAP, which was previously used to visualize particle orientations by Lin and Ng[20] (see their Fig. 8), has the advantage of preserving the number density of the projected points over the flat surface. Two typical cases are shown in Fig. 5, both of $\phi = 0.40$. For both cases, the initial distribution of particle orientation is relatively more random with some preference towards 90° and 270° (T_3) angles, which is a result of the initialization scheme[28] at this large value of ϕ. As the shear strain ($\dot{\gamma}t$) increases, the particles in the $\alpha = 0.4$ case notably migrate towards the center of the circle, which corresponds to a particle with normal vector aligned with the y-axis (T_2). Particles are observed to reorient such that their normal vectors are more aligned with the direction of the velocity gradient, which is consistent with the findings by numerical simulations[9,14] and laboratory measurement[30]. For comparison, in the case with $\alpha = 0.8$, no systematic reorientation of the particles is observed. Having inspected all simulations, we found no such reorientation for cases of $\alpha = 1.0$ or 0.8, where the particles are spherical or too close to a sphere. Presumably, the reorientation is a consequence of inter-particle collisions. Therefore, one may expect the reorientation to be more likely for denser suspensions. Indeed, for $\alpha = 0.6$, systematic reorientation occurs for $\phi \geq 0.30$; for $\alpha = 0.4$, it occurs for $\phi \geq 0.15$.

The behavior of N_1^*, which is presented in Fig. 4(a), may be linked to the particle reorientation shown in Fig. 5(a-c). According to the results from particle pair interactions[3], N_1^* is expected to be negative. It was also found recently that wall confinement[31,32] could be the main contributor to the normal stress in the wall-normal direction, leading to positive N_1^*. A consequence of the

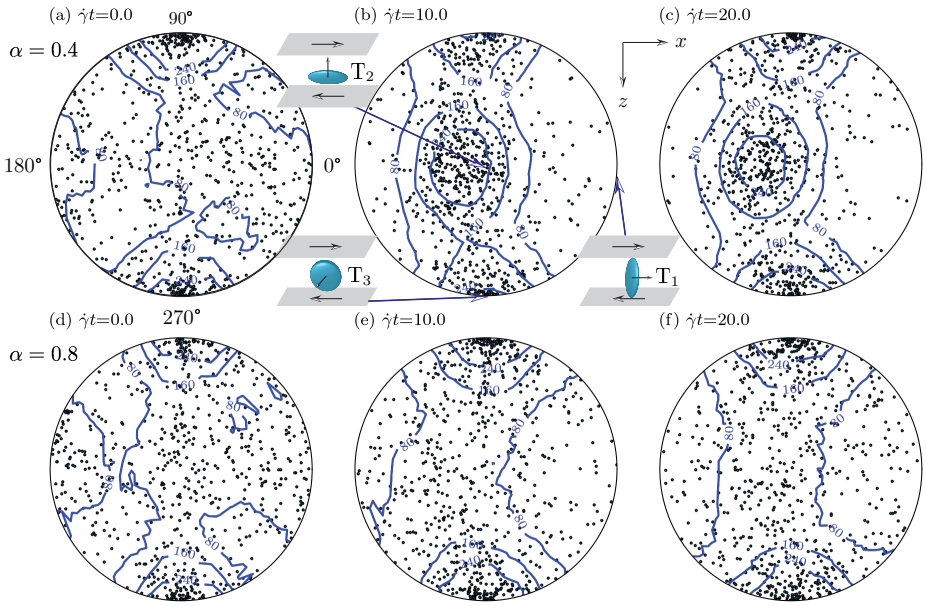

FIG. 5: Equal area projection of particle normal vector $\boldsymbol{n}$ (Fig. 1(b)) onto the x-z plane for the cases with (a–c) $\alpha = 0.4$ and (d–f) $\alpha = 0.8$, both at $\phi = 0.40$ and for various strain ($\dot{\gamma}t$). The contour lines show the particle's number density over the projection plane. Three types of particles, whose $\boldsymbol{n}$ points at x-, y- and z-axes respectively, are labelled as T_1, T_2 and T_3 for illustration.

particle reorientation could be that the oblate particle suspension is not as effective in transmitting the normal stress in the wall-normal y direction as the spherical case, because the longer axes of the particles become more parallel to the walls, i.e., closer to the T_2 orientation shown in Fig. 5(b). As a result, the wall confinement effects are expected to be weaker for the more oblate particle suspensions, which could be the reason for the sign change in N_1^* observed in Fig. 4(a) as α decreases from 1.0 to 0.4. In particular, N_1^* for the $\alpha = 0.4$ case (Fig. 4(a)) becomes more negative at larger volume fraction ϕ, which is presumably due to increased particle pair interactions[3] and weakened wall confinement effects[31,32].

Some micro-structural statistics for particle contacts are presented in Fig. 6. First, the dimensionless contact distance, R_d (see Fig. 1(b)), averaged for all contact pairs in each simulation, is plotted in Fig. 6(a) as a function of ϕ. For the sphere case ($\alpha = 1$), R_d is unity by definition. For all oblate cases ($\alpha < 1$), R_d is observed to be greater than unity, suggesting that the average contact distance has been increased from the sphere case of the same equivalent radius r^* (Fig. 1). Moreover, at a given ϕ, R_d increases as the particle becomes more oblate (i.e., as α decreases). In Fig. 6(b), the contact ratio R_c, i.e., the average number of contacts per particle, can be seen to

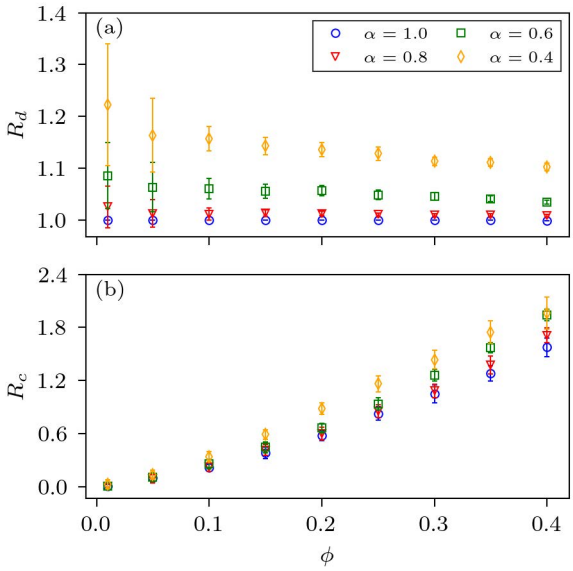

FIG. 6: The average (a) contact distance R_d and (b) contact ratio R_c plotted against ϕ.

increase with ϕ, which is as expected. In general, R_c also increases as α decreases. The latter trend was also reported by Donev *et al.*[33] in their study of maximum packing fraction for non-spherical particles, which was attributed to the increase of the degrees of freedom as the particle shape becomes less isotropic. The same mechanism could take place in the shear flow, although the volume fraction ϕ is smaller than those studied by Donev *et al.*[33] The increase of R_c implies a higher likelihood for momentum transfer to occur due to inter-particle collisions and thus a higher viscosity, which is in agreement with the trend observed in Fig. 3 between viscosity and the control parameters, i.e., ϕ and α. In short, inter-particle collisions are found to be more frequent on a per-particle basis in the more oblate particle suspensions, which is consistent with the observed increase of viscosity with decreasing α (Fig. 3).

TABLE IV: Parameters for the best fit of KD model. Data for $\alpha = 0.13$ (bottom row) are obtained from Mueller et al.[8]

α	ϕ_m	B	R^2
1.00	0.64	2.46	0.994
0.80	0.70	2.65	0.999
0.60	0.71	2.79	0.998
0.40	0.68	2.80	0.989
0.13	0.62	3.17	0.998

In order to compile the viscosity data in Fig. 3, we formulate the best fits directly to the viscosity laws. Specifically for the KD model, one could find the best fit for both ϕ_m and B. Instead, we use the experimental results[33] to obtain the maximum packing fraction ϕ_m for each α and fit the KD model to our data (Fig. 3(a)) to obtain the Einstein coefficients, B. Such results are tabulated in Table IV and can complement an earlier result[8] for $\alpha = 0.13$ (see their Table 3). It can be seen that ϕ_m reaches the maximum at $\alpha \approx 0.60$[33] and B decreases monotonically with increasing α.

In conclusion, we have presented the rheological properties of oblate particle suspensions for a considerable range of volume fraction and aspect ratio. Other than these two parameters, there could be numerous other factors in determining the rheology which have been studied recently[34–37] for spherical particle suspensions. Investigating these effects for non-spherical particle suspensions, as well as extending the simulations to even denser suspensions, could be avenues for future research.

Acknowledgements The support from the Natural Sciences and Engineering Research Council of Canada (NSERC) is gratefully acknowledged. This research was enabled in part by support provided by Compute Canada (www.computecanada.ca). The initial random packing of the ellipsoids is generated by the software *Packing Ellipsoid 3* kindly provided by Dr. R. D. Lobato. We thank two anonymous referees whose constructive comments helped us improve the paper significantly.

REFERENCES

[1]J. J. Stickel and R. L. Powell, "Fluid mechanics and rheology of dense suspensions," Annual Review of Fluid Mechanics **37**, 129–149 (2005).

[2]M. M. Denn and J. F. Morris, "Rheology of non-Brownian suspensions," Annual Review of Chemical and Biomolecular Engineering **5**, 203–228 (2014).

[3]E. Guazzelli and O. Pouliquen, "Rheology of dense granular suspensions," Journal of Fluid Mechanics **852**, P1 (2018).

[4]A. Einstein, "Eine neue bestimmung der moleküldimensionen," Annalen der Physik **324**, 289–306 (1906).

[5]G. Batchelor and J. Green, "The determination of the bulk stress in a suspension of spherical particles to order c^2," Journal of Fluid Mechanics **56**, 401–427 (1972).

[6]T. Kitano, T. Kataoka, and T. Shirota, "An empirical equation of the relative viscosity of polymer melts filled with various inorganic fillers," Rheologica Acta **20**, 207–209 (1981).

[7]W. Pabst, E. Gregorová, and C. Berthold, "Particle shape and suspension rheology of short-fiber systems," Journal of the European Ceramic Society **26**, 149–160 (2006).

[8]S. Mueller, E. W. Llewellin, and H. M. Mader, "The rheology of suspensions of solid particles," Proceedings of the Royal Society A **466**, 1201–1228 (2010).

[9]E. Bertevas, X. Fan, and R. I. Tanner, "Simulation of the rheological properties of suspensions of oblate spheroidal particles in a Newtonian fluid," Rheologica Acta **49**, 53–73 (2010).

[10]J. E. Butler and B. Snook, "Microstructural dynamics and rheology of suspensions of rigid fibers," Annual Review of Fluid Mechanics **50**, 299–318 (2018).

[11]S. H. Maron and P. E. Pierce, "Application of Ree-Eyring generalized flow theory to suspensions of spherical particles," Journal of Colloid Science **11**, 80–95 (1956).

[12]I. M. Krieger and T. J. Dougherty, "A mechanism for non-Newtonian flow in suspensions of rigid spheres," Journal of Rheology **3**, 137–152 (1959).

[13]G. Jeffery, "The motion of ellipsoidal particles in a viscous fluid," Proceedings of the Royal Society A **102**, 58–61 (1922).

[14]Q. Meng and J. J. L. Higdon, "Large scale dynamic simulation of plate-like particle suspensions. part I: Non-Brownian simulation," Journal of Rheology **52**, 1–36 (2008).

[15]M. J. Krause, F. Klemens, T. Henn, R. Trunk, and H. Nirschl, "Particle flow simulations with homogenised lattice Boltzmann methods," Particuology **34**, 1–13 (2017).

[16]R. Trunk, J. Marquardt, R. Thäter, H. Nirschl, and M. Krause, "Towards the simulation of arbitrarily shaped 3D particles using a homogenised lattice Boltzmann method," Computers & Fluids **172**, 621–631 (2018).

[17]M. J. Krause, A. Kummerländer, S. J. Avis, H. Kusumaatmaja, D. Dapelo, F. Klemens, M. Gaedtke, N. Hafen, A. Mink, R. Trunk, J. E. Marquardt, M.-L. Maier, M. Haussmann, and S. Simonis, "OpenLB—Open source lattice Boltzmann code," Computers & Mathematics with Applications **81**, 258–288 (2020).

[18]A. J. C. Ladd, "Numerical simulations of particulate suspensions via a discretized Boltzmann equation. part 1. theoretical foundation," Journal of Fluid Mechanics **271**, 285–309 (1994).

[19]A. Ladd, "Numerical simulations of particulate suspensions via a discretized Boltzmann equation. Part 2. Numerical results," Journal of Fluid Mechanics **271**, 311–339 (1994).

[20]X. Lin and T.-T. Ng, "A three-dimensional discrete element model using arrays of ellipsoids," Géotechnique **47**, 319–329 (1997).

[21]X. Lin and T.-T. Ng, "Contact detection algorithms for three-dimensional ellipsoids in discrete element modelling," International Journal for Numerical and Analytical Methods in Geomechanics **19**, 653–659 (1995).

[22]K. L. Johnson, *Contact Mechanics* (Cambridge University Press, 1985).

[23]S. Gallier, E. Lemaire, F. Peters, and L. Lobry, "Rheology of sheared suspensions of rough frictional particles," Journal of Fluid Mechanics **757**, 514–549 (2014).

[24]Z. Zhou, D. Pinson, R. Zou, and A. Yu, "Discrete particle simulation of gas fluidization of ellipsoidal particles," Chemical Engineering Science **66**, 6128–6145 (2011).

[25]Y. Thorimbert, F. Marson, A. Parmigiani, B. Chopard, and J. Lätt, "Lattice boltzmann simulation of dense rigid spherical particle suspensions using immersed boundary method," Computers & Fluids **166**, 286–294 (2018).

[26]T. Krüger, *The Lattice Boltzmann Method* (Springer International Publishing, 2017).

[27]J. Guo, *Direct simulations of fluid-particle flow in Newtonian and non-Newtonian fluids using coupled lattice Boltzmann and discrete element methods*, Ph.D. thesis, University of Calgary (2021).

[28]E. G. Birgin and R. D. Lobato, "A matheuristic approach with nonlinear subproblems for large-scale packing of ellipsoids," European Journal of Operational Research **272**, 447–464 (2019).

[29]N. I. Fisher, T. Lewis, and B. J. Embleton, *Statistical Analysis of Spherical Data* (Cambridge University press, 1993).

[30]A. B. D. Brown, S. M. Clarke, P. Convert, and A. R. Rennie, "Orientational order in concentrated dispersions of plate-like kaolinite particles under shear," Journal of Rheology **44**, 221–233 (2000).

[31]T. Dbouk, L. Lobry, and E. Lemaire, "Normal stresses in concentrated non-Brownian suspensions," Journal of Fluid Mechanics **715**, 239 (2013).

[32]S. Gallier, E. Lemaire, L. Lobry, and F. Peters, "Effect of confinement in wall-bounded non-colloidal suspensions," Journal of Fluid Mechanics **799**, 100–127 (2016).

[33]A. Donev, I. Cisse, D. Sachs, E. A. Variano, F. H. Stillinger, R. Connelly, S. Torquato, and P. M. Chaikin, "Improving the density of jammed disordered packings using ellipsoids," Science **303**, 990–993 (2004).

[34]L. Lobry, E. Lemaire, F. Blanc, S. Gallier, and F. Peters, "Shear thinning in non-Brownian suspensions explained by variable friction between particles," Journal of Fluid Mechanics **860**, 682–710 (2019).

[35]A. Papadopoulou, J. J. Gillissen, H. J. Wilson, M. K. Tiwari, and S. Balabani, "On the shear thinning of non-Brownian suspensions: Friction or adhesion?" Journal of Non-Newtonian Fluid Mechanics **281**, 104298 (2020).

[36]Y. Lin, Y. Wang, H. Qin, D. Pan, and J. Chen, "Surface roughness effect on the shear thinning of non-colloidal suspensions," Physics of Fluids **33**, 043104 (2021).

[37]Y. Lin, Y. Wang, Z. Weng, D. Pan, and J. Chen, "Air bubbles play a role in shear thinning of non-colloidal suspensions," Physics of Fluids **33**, 011702 (2021).